A Fast and High-Performance Self-Powered Photodetector Based on ZnO/Metal-Organic Framework Heterojunction

Yingyi Wang[1,2,3#], Lin Liu[2#], Yixiang Shi[4], Shengzhao Li[2], Fuqin Sun[2], Qifeng Lu[5], Yaochun Shen[3], Simin Feng[2*], Sujie Qin[1*]

1 Department of Health and Environmental Sciences, Xi'an Jiaotong-Liverpool University, 111 Ren'ai Road, Suzhou, Jiangsu, 215123, P. R. China

2 i-Lab, Key Laboratory of Multifunctional Nanomaterials and Smart Systems, Suzhou Institute of Nano-Tech and Nano-Bionics (SINANO), Chinese Academy of Sciences (CAS), Suzhou, Jiangsu, 215123, P. R. China

3 Department of electrical engineering and electronics,, University of Liverpool, Brownlow Hill, Liverpool L69 7ZX, United Kingdom

4 Department of Chemistry, The University of Hong Kong, Pokfulam Road, Hong Kong, P. R. China

5 School of CHIPS, XJTLU Entrepreneur College (Taicang), Xi'an Jiaotong-Liverpool University, 111 Taicang Avenue, Taicang, Suzhou, Jiangsu 215488, P. R. China

#Y. W. and L. L. are co-first author.

Correspondence should be addressed to S.F.(email: smfeng2020@sinano.ac.cn)，or S.Q. (email: sujie.qin@xjtlu.edu.cn)

Abstract

Electrical conductive metal-organic frameworks (EC-MOFs) are emerging as an appealing class of highly tailorable electrically conducting materials with potential applications in optoelectronics. Here, we *in-situ* grew nickel hexahydroxytriphenylene (Ni-CAT) on the surface of ZnO nanorods (NRs). The self-powered photodetectors (PDs) were fabricated with heterojunctions formed at the interface of ZnO NRs and Ni-CAT. With this, the built-in electric field (BEF) can effectively separate the photogenerated electron-hole pairs and enhance the photoresponse. We observe that the PDs based on hybrid ZnO/Ni-CAT with 3 hours growth time (ZnO/Ni-CAT-3) show good photoresponse (137 μA/W) with the fast rise (3 ms) and decay time (50 ms) under 450 nm light illumination without biased voltage. This work provides a facile and controllable method for the growth of ZnO/Ni-CAT heterojunction with effective BEF zone, which will benefit their optoelectronic applications.

Introduction

Metal-organic frameworks (MOFs) are a class of porous materials formed by coordination bonding between metal ions and organic ligands.[1] Since their discovery, they have attracted increasing attention in various fields, such as gas adsorption and separation, catalysis, and protection or filtration film, due to their high porosity, high specific surface area, and tunable functionality.[2-7] However, the majority of MOFs are insulators with low conductivity, which limits their application in the optoelectronic field because of their strong charge localization and low electron density.[8] Electrically conductive MOFs (EC-MOFs) are a class of MOFs with the intrinsic ability of electronic conduction, which could be regarded as a potential material in the electronic or optoelectronic field because of their controllable conductivities and unique inorganic-organic structure.[9-12]

EC-MOFs with diverse crystal structures and controllable conductivities have demonstrated promising performance in optical electronics.[13, 14] Carrier mobility and

bandgaps are two key parameters that influence their optoelectronic performances. Two-dimensional (2D) layered EC-MOFs, where metal ions and organic ligands form extended π-conjugation, exhibit high charge-carrier mobility and conductivity.[15] In addition, most 2D EC-MOFs exhibit narrow band gap, which benefits their applications in broadband optoelectronics. For example, Arora, et al.[9] grew a semiconducting $Fe_3(THT)_2(NH4)_3$ (THT: 2,3,6,7,10,11-triphenylenehexathiol) 2D MOF ($Fe_3(HTTP)_2$) via a liquid-liquid (ethyl acetate/water) interface growth method which would tune the interface bonding between the substrate and the sensing material. The $Fe_3(HTTP)_2$-based PDs are capable of detecting a broad wavelength range from UV to NIR (400–1575 nm) under -1 V bias voltage. Although significant improvements in the performance of the device are achieved, it exhibits the drawbacks of long rise time, low photo-responsibility, and high energy consumption. Similarly, Sun, et al.[16] developed a single crystal Cu-BTC (where BTC is benzene-1,3,5-tricarboxylate) MOF material in an ethanol-water mixture solution, which showed a potential photo-sensing property under high bias voltage (10 V). However, these 2D EC-MOFs based PDs usually need high bias voltage to efficiently separate the charges.[17]

Establishing the built-in electric field (BEF) of heterojunction can efficiently promote the separation of photogenerated charges and fabricate self-powered PDs by harvesting energy from light irradiation.[18-20] Meanwhile, the in-situ growth of heterojunctions provides the possibility to enhance the interface interconnection and facilitate the transportation of carriers.[21] Thus, n-type ZnO, as a widely used photo-sensing material with a work function of 4.0 eV and a bandgap of 3.31 eV, is selected as a template for in-situ growth p-type nickel hexahydroxytriphenylene ($Ni_3(HHTP)_2$, Ni-CAT; work function, 5.0 eV; bandgap, 2.68 eV).[22] Several works have been researched on metal oxides as the template for bottom-up self-assembly MOFs. For example, Zhan, et al.[23] reported ZnO@ZIF-8 core-shell heterostructures by the self-template method. However, because of the relatively low conductivity of ZIF-8, the PDs require external bias voltage (-5 V) and show a slow rise and decay time.

Herein, we select nickel hexahydroxytriphenylene (Ni-CAT) MOF material with higher electrical conductivity and in-situ grew it on the surface of ZnO nanorods (NRs) to establish a BEF and design a self-powered PDs. The thickness and coverage area of Ni-CAT on the ZnO surface is controlled by tuning the growth time. Benefiting from the formed BEF between ZnO NRs and Ni-CAT, the photo-sensing performance of ZnO/Ni-CAT heterojunction-based PDs exhibited significant improvement compared with ZnO-based PD at zero bias. Under 3 hours of growth time (ZnO/Ni-CAT-3), the device showed the highest photo response with a fast response time of 3 ms under 450 nm light illumination without a bias voltage. The new design strategy enables us to develop fast, high-performance, self-powered broadband PDs.

Experiment Section

Materials and Synthesis of Composites

Ethyl alcohol (AR), Acetone (AR), $Zn(CH_3COO)_2$ (AR), $Al(NO)_3$ (AR), $Zn(NO_3)_2 \cdot 6H_2O$ (AR) was purchased from Shanghai Hushi Laboratorial Equipment Co., Ltd; $C_6H_{12}N_4$ (AR) and $Ni(CH_3COO)_2$ (AR) was purchased from Sigma Aldrich; 2,3,6,7,10,11-hexahydroxytriphenylene (HHTP) ligand was purchased from J&K Scientific. These reagents were used without any further purification.

The ZnO/Ni-CAT hybrid heterojunctions were prepared via a synthetic process illustrated in Figure S1. Initially, the seed solution, 20 mM $Zn(CH_3COO)_2$ and 10 mM $Al(NO)_3$ of the ethyl alcohol, was spin-coated (3000 rpm, 20 s) on the Si/SiO$_2$ substrates and annealed in air at 400°C for 30 min to form ZnO seed layer. Then, the seed layer was immersed into 25 mM $C_6H_{12}N_4$ and $Zn(NO_3)_2 \cdot 6H_2O$ solution kept at 85°C for 5h to obtain ZnO NRs. Later, the Ni-CAT was in-situ grown on the surface of ZnO NRs in the mixture solution of 80 µM 2,3,6,7,10,11-hexahydroxytriphenylene (HHTP) ligand and 160 µM $Ni(CH_3COO)_2$. The growth temperature was kept constant at 85°C and the growth time varied between 1-5 hours (the corresponding products were defined as ZnO/Ni-CAT-1, ZnO/Ni-CAT-3, and ZnO/Ni-CAT-5 for 1 h, 3 h and 5 h

respectively). Finally, the synthesized ZnO/Ni-CAT composites were activated by washing with deionized water and acetone three times, followed by evacuating under a vacuum at 85℃ for 12 h to remove possible guest molecules.

Sensor fabrication

As shown in Figure.S2, the sensor contains three parts: a bottom electrode (Cr (15 nm)/Au (100 nm)), ZnO/Ni-CAT heterojunctions, and a top electrode (Ag paste). Firstly, the Si/SiO$_2$ substrate was cleaned by acetone, ethanol, and deionized water sequentially and dried with nitrogen gas. Afterward, the bottom electrodes (Cr/Au) were deposited on the Si/SiO$_2$ substrate by traditional photolithography (MA6-1), sputtering (FHR), and the lift-off method. Then the substrate was used to grow ZnO NRs and Ni-CAT in situ by the hydrothermal method as previously explained. Finally, a solution of Ag paste was applied to the active areas, and the sample was subjected to curing on a hot plate at 60℃ for 2 h.

Characterization of Composites and Microstructures

The morphology of ZnO/Ni-CAT composites were analyzed by scanning electron microscopy (SEM, Hitachi-Regulus 8230) and transmission electron microscopy (TEM, Tecnai G2 F20 S-Twin). The chemical composition of materials was carried out by energy dispersive spectrometry (EDS, Hitachi- Regulus 8230), and the crystal structure was analyzed by X-ray Diffraction with Cu-Kα radiation (λ = 1.5405 Å) (XRD, Bruker AXS, D8 Advance). The surface composition and electronic states of the elements were investigated by X-ray photoelectron spectroscopy (XPS, Smartlab(3KW) Japan Rigaku).

Measurements

All measurements were carried out under ambient conditions, and the dark currents were measured in a dark box to eliminate the influence of ambient light. The

LED light source (UVEC-4, Shenzhen LAMPLIC TECH Co., Ltd) with adjustable light power density was used to illuminate the sample. Electrical and Photoelectrical measurements were performed with Agilent B1500A.

Results and Discussion

Characterization

The SEM images of the morphology of synthesized ZnO NRs and ZnO/Ni-CAT composites are shown in Figure 1 and Figure S2. The hexagonal ZnO NRs are uniformly grown on the silicon substrate with an average height of around 2.5 μm (Figure 1a, Figure S3). To enhance the interface interconnection between ZnO NRs and Ni-CAT and facilitate the transportation of carriers, Ni-CAT was in situ grown on the surface of the ZnO NRs. Figure 1b demonstrates that the ZnO NRs template was fully covered with Ni-CAT-3. We observe that the size and density of Ni-CAT gradually increased by comparing the SEM images of ZnO/Ni-CAT-1 and ZnO/Ni-CAT-5 composites (shown in Figure S4a, b), which can increase the number of effective carrier transport channels. When the growth time is 1h, most of the Ni-CAT-1 was grown on the top of ZnO NRs (Figure S4a). When the growth time extends to 5 h, the Ni-CAT not only densely grew on the surface of ZnO NRs but also filled in the spaces between ZnO NRs (Figure S4b). Moreover, cracks started to generate on the ZnO/Ni-CAT-5 film due to the increased crystal size and amount of Ni-CAT. The low magnification TEM image of ZnO/Ni-CAT-3 (as shown in Figure 1c) clearly demonstrates that the Ni-CAT was grown on the surface of ZnO. The high-resolution TEM (HRTEM) image (Figure 1d) of the Ni-CAT shows a characteristic lattice fringe pattern of 1.83 nm, which belongs to the (100) lattice plane of the Ni-CAT hexagonal crystal system. The selected area electron diffraction pattern (SAED) (bottom inset of Figure 1f) also confirms the high degree crystallinity of Ni-CAT. The EDS spectra (Figure 1e) and mapping images (Figure 1f) clearly show that the ZnO/Ni-CAT-3 composites contain C, O, Zn, Ni, and Al elements. The atomic ratio of Ni/Zn increases from 0.24 to 0.83

by increasing the growth time from 1 h to 5 h (Figure 1e and Figure S4c, d), indicating more Ni-CAT was produced which agrees with the morphology results of ZnO/Ni-CAT composites in SEM images.
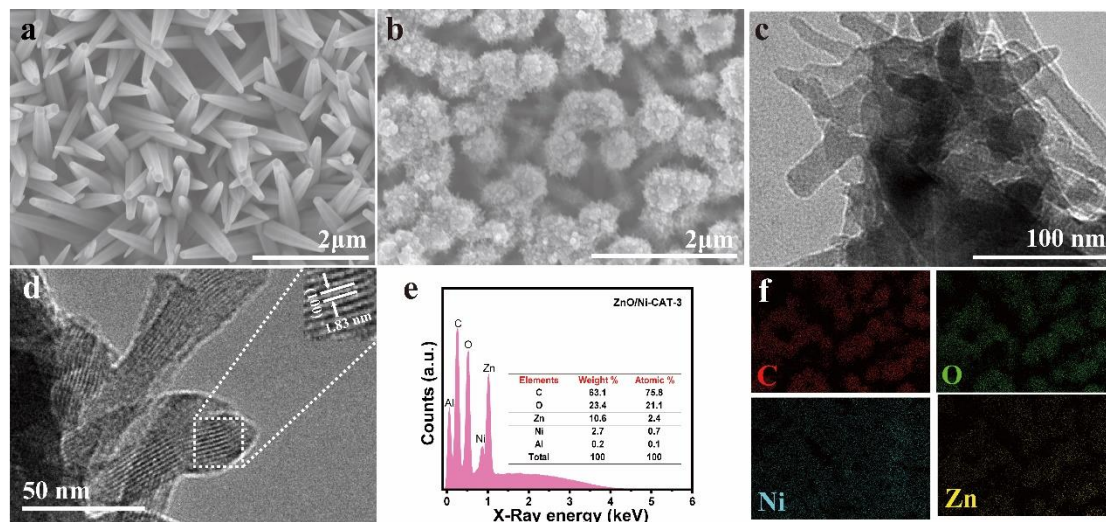

Figure 1. SEM image of (a) ZnO/Ni-CAT-0 and (b) ZnO/Ni-CAT-3; (c) Low magnification TEM image of ZnO/Ni-CAT nanostructure; (d) HRTEM image of ZnO/Ni-CAT nanostructure (top inset: corresponding lattice fringe pattern; bottom inset: selected area electron diffraction pattern); (e) Qualitative EDS spectrum of ZnO/Ni-CAT-3; (f) Elemental mapping of ZnO/Ni-CAT-3 with the different atom.

Next, we focus on the crystal structure of the ZnO/Ni-CAT composites. As shown in Figure 2a, the XRD pattern characterization reveals that the ZnO/Ni-CAT composites are successfully synthesized. The Al_2O_3 peaks were generated from the seed layer and Si/SiO_2 peaks were generated from the substrate (Figure S5). The diffraction peaks at $2\theta = 31.88°$, $34.54°$, $36.38°$, and $47.64°$ can be indexed to the (100), (002), (101), and (102) planes of hexagonal phase ZnO (JCPDS NO. 36-1451). The other diffraction peaks at $2\theta = 4.7°$ and $9.3°$ correspond to the (100) and (200) planes of the simulated Ni-CAT crystal structure (Figure S5) and demonstrate hexagonal packing of Ni-CAT within the ab planes. The intensities of these Ni-CAT peaks increased with the increase of growth time and reached the maximum for ZnO/Ni-CAT-5 sample, as

shown in Figure 2a. It is noted that diffraction peaks of ZnO shift to a higher degree (0.22°) with increasing Ni-CAT due to the introduction of defects during the growth.

XPS is a powerful tool to provide the chemical and bonding information of the sample surfaces. The XPS spectra of ZnO/Ni-CAT composites are displayed in Figure 2b-e. The XPS survey spectrum shows that the ZnO/Ni-CAT heterojunctions contain only C, O, Ni and Zn without any other elements, indicating the high purity of as-grown ZnO/Ni-CAT composites (Figure S6, Figure S7, and Figure S8). Regarding the high-resolution C 1s spectrum, it can be fitted into four curves with peaks at 284.8, 286.5, 288.3, and 290.7 eV, which can be ascribed to the C-O, C=O, C=C bonds and $\pi-\pi^*$ satellite peaks that originate from the triphenylene ring of the HHTP ligand, respectively (Figure 2b).[24] The O 1s XPS spectrum can also be deconvoluted into five peaks at 531.0, 531.7, 532.0, 533.0, and 535.3 eV for lattice oxygen (ZnO), C=O, Ni-O, C-O and H_2O, respectively (Figure 2c). The characteristic peaks of Zn $2p_{3/2}$ and Zn $2p_{1/2}$ are located at 1022.09 and 1045.19 eV, respectively (Figure 2d). Moreover, the Ni $2p_{3/2}$ and Ni $2p_{1/2}$ peaks are located at 856.3 and 874.1 eV, respectively, as well as two shake-up satellite peaks (denoted as "Sat.") at 861.5 and 880.5 eV (Figure 2e). The binding energy of difference between Ni $2p_{1/2}$ and $2p_{3/2}$ peaks is 17.9 eV, and between Zn $2p_{1/2}$ and $2p_{3/2}$ peaks is 23.1 eV, which reveals that both the Ni and Zn ions were present in the divalent state in ZnO/Ni-CAT heterojunctions.[25-27]
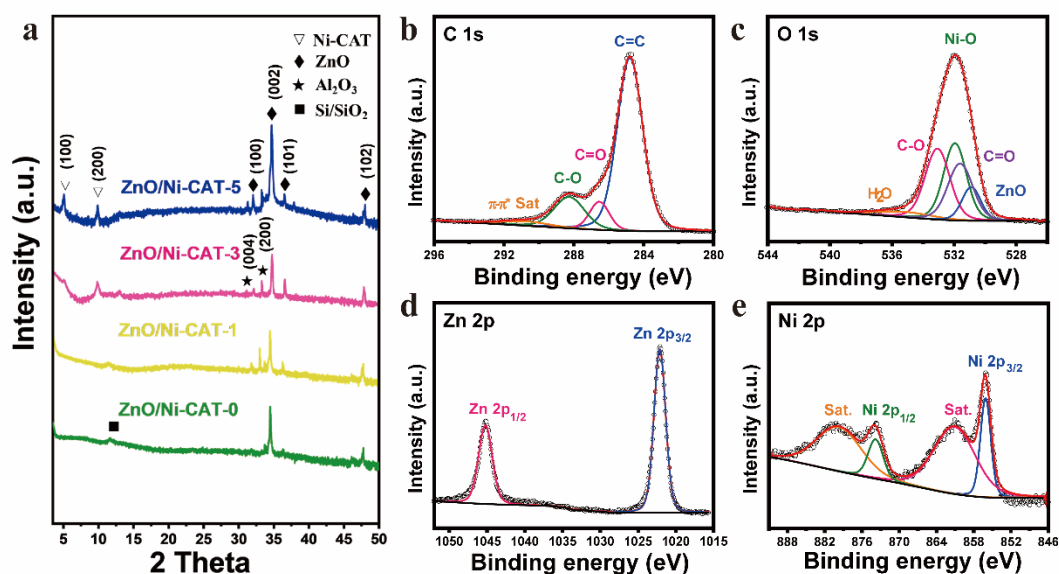
Figure 2. (a) XRD patterns of pristine ZnO and ZnO/Ni-CAT heterojunctions; (b-e) XPS spectra of C 1s, O 1s, Zn 2p and Ni 2p of the ZnO/Ni-CAT heterojunction samples, respectively.

Photodetector performance

The photo-sensing performance of the ZnO/Ni-CAT heterojunction based PDs was evaluated by measuring the current-time curves under different illumination conditions. The photoresponse is calculated as below:

$$Response = \frac{I_P - I_D}{PS} \tag{1}$$

where I_P, I_D, P, and S stand for photocurrent, dark current, light power density, and effective contact area (except the electrodes blocking area), respectively.[28] Figure 4a shows the photoresponse of three PDs at zero bias voltage under different light illumination conditions ($P = 5$ mW cm^{-2}, $\lambda = 365, 420, 450, 500, 600,$ and 800 nm). We observe that the pure ZnO NRs (ZnO/Ni-CAT-0) based PD shows a moderate photoresponse towards light illumination. This is because a BEF would form between the fabricated two asymmetric electrodes (Ag and Au electrode, respectively), and photogenerated carriers can separate and transport by this, leading to a noteworthy photoresponse. Regarding ZnO/Ni-CAT based PDs with different growth times, we found out that the photoresponse of the ZnO/Ni-CAT-3 based PD increases from 98.4 to 132.5 µA W^{-1} with increasing wavelengths from 365 to 450 nm, while it drops to 71.4 µA W^{-1} when the light wavelength further increases to 800 nm. The PD fabricated with ZnO/Ni-CAT-3 shows the highest photoresponse (132.5 µA W^{-1}) under 450nm light illumination, which is 27.6 times larger than that of ZnO/Ni-CAT-0 based PD (4.8 µA W^{-1}), and 10^4 times larger than that of ZnO/Ni-CAT-1 and ZnO/Ni-CAT-5 based PDs (0.012 µA W^{-1}). This is because, for ZnO/Ni-CAT-1 based PDs, the Ni-CAT nanoneedles do not fully cover the surface of ZnO NRs and a discontinuous p-n heterojunction was formed between ZnO and Ni-CAT (Figure S2). Therefore, the photogenerated carriers cannot efficiently separate and transport to the two asymmetric

electrodes (Figure 3a). When the growth time further increases to 5h, the thickness of the Ni-CAT layer increases and the spaces between ZnO NRs are filled with Ni-CAT nanoneedles and cracks start to produce. Therefore, the photoresponse of ZnO/Ni-CAT-5 based PDs reduces as fewer photos can reach the interface of ZnO/Ni-CAT owing to the thick Ni-CAT layer.

Figure 3b shows the current-voltage (I-V) curves of the ZnO/Ni-CAT-3 based PDs in the dark and different illumination conditions (with illumination light wavelength from 365nm to 800nm, P = 5.7 mW cm^{-2}). It demonstrates that the ZnO/Ni-CAT-3 based PDs have a typical rectification characteristic, suggesting a well-behaved diode structure owing to the formed p-n heterojunction. Upon light exposure (λ = 450 nm), the current of the device dramatically increases from the OFF state to the steady ON state within 3 ms at zero bias (Figure 3c) and it takes 50 ms for the device to return to the OFF state, which is faster than the rise and decay time of ZnO/Ni-CAT-0, ZnO/Ni-CAT-0 and ZnO/Ni-CAT-0 based PDs (Figure S10). The rise time (decay time) is defined as the time interval between the response rising (descending) from 10% (90%) to 90% (10%) of the peak current density. The fast response time of PDs at zero bias originated from the rapid separation and the transport speed of the photogenerated charge carriers due to the established BEF within the heterojunctions.[29, 30] The ON/OFF ratios of the device are around 10^2 with 5.69 mW cm^{-2} power density. The periodic illuminations testing of the ZnO/Ni-CAT-3 based PDs is demonstrated by a series of stable and repeatable photoresponse under the irradiation of 450 nm light at zero bias (P = 5.7 mW cm^{-2}, Figure 3d).
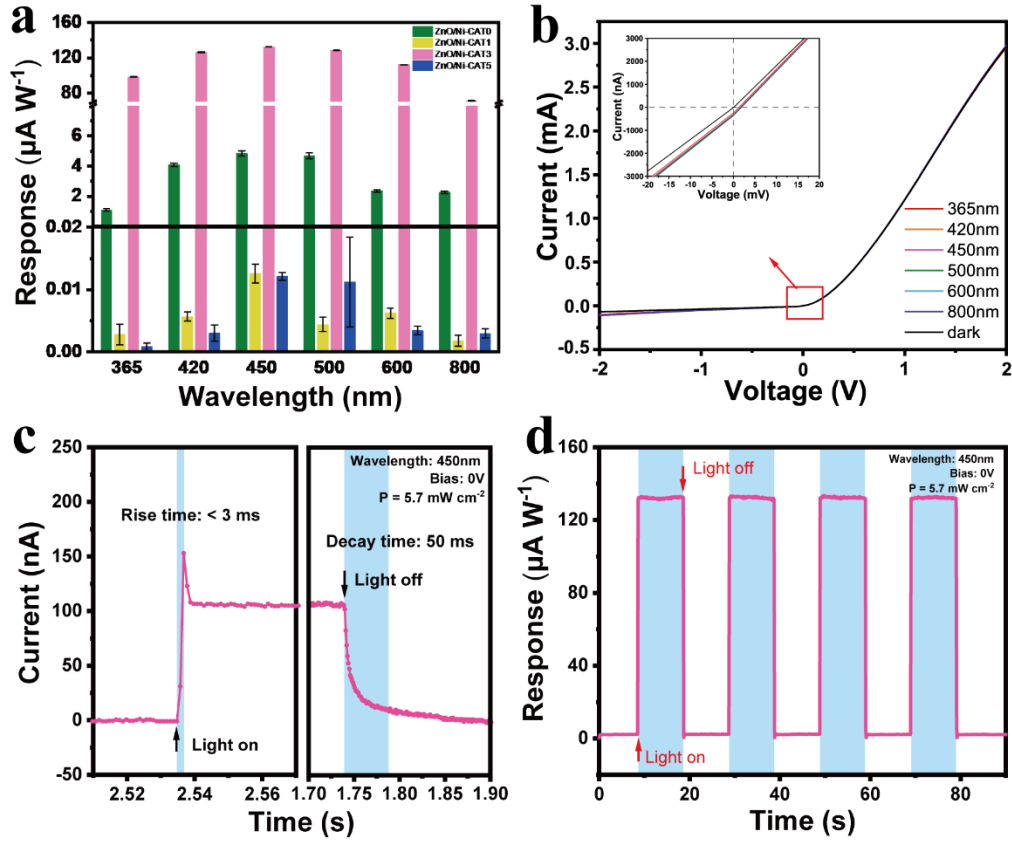
Figure 3. (a) Wavelength-dependent photoresponse of ZnO/Ni-CAT-3 heterojunction based self-powered PDs; (b) I–V curves of the ZnO/Ni-CAT-3 based PDs in dark and under various wavelengths (from 365 to 800 nm) of visible light; (c) Rise-fall time curve for ZnO/Ni-CAT-3 illuminated with 450 nm visible light at zero bias voltage; (d) Photoresponse of ZnO/Ni-CAT-3 under 450 nm periodic illuminations zero bias voltage.

The dynamic photoresponse of ZnO/Ni-CAT-3 based PD under zero bias was also tested (Figure 4a). When the light power density changes from 5.7 to 51.0 mW cm^{-2}, the photoresponse of the PD linearly increases and achieves the highest photocurrent of 278.9 µA W^{-1} at 51.0 mW cm^{-2}. This is because the power density of light is proportional to the number of photons when the wavelength of the light is a constant according to Equation (2),[28]

$$PS = \frac{Nhc}{\lambda} \qquad (2)$$

where N is the number of incident photons, h is the Planck's constant, c is the speed of light, and λ is the wavelength of the incident light. An increase in power density would increase the number of photogenerated charge carriers, resulting in an enhancement of the photocurrent.[28] Figure 4b illustrates the photoresponse of the ZnO/Ni-CAT-3 based PD as a function of illumination intensity at zero bias. It indicated that the photoresponse drastically decreases with the increase of power density due to the increased recombination rate of the photoexcited carriers.[29, 31-33]

For a clear comparison, Table 1 summarizes the relevant parameters of recently published MOF-based PDs compared to our work. It shows that our work reveals the superiority of a fast response and recovery speed at zero bias with high photoresponse of ZnO/Ni-CAT-3 based PDs.
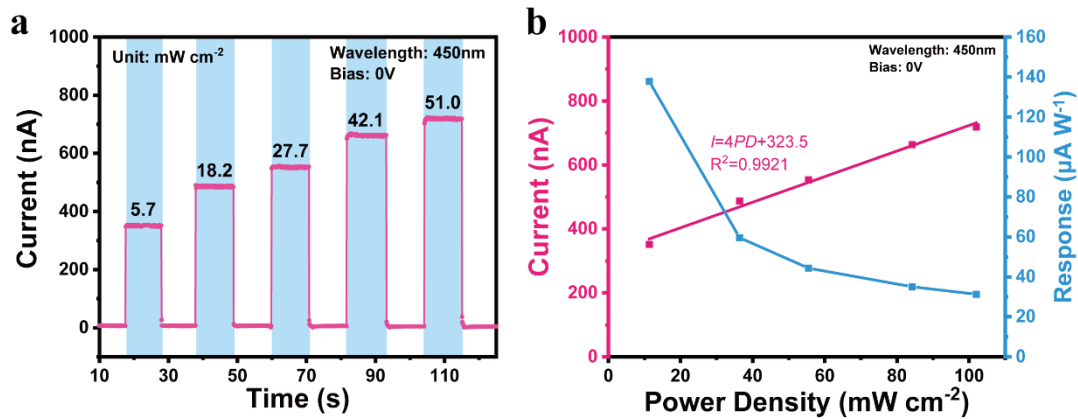

Figure 4. (a) Photoswitching characteristics of the ZnO/Ni-CAT-3 devices under various light intensities at zero bias voltage. (b) Light-intensity dependence of the photocurrent and photoresponse under 450 nm illumination of the ZnO/Ni-CAT-3 devices.

Table 1. Performance comparison of recently developed MOF based PDs.

Devices	Rise/decay time (s)	Bias (V)	Response ($\mu A\ W^{-1}$)	Wavelength (nm)	Ref.
Fe_3HTTP_2 MOF	2.3/2.15	-1V	-	785	[9]
Co-$CoO_x/NC/Mo_2CT_x$	0.4/0.4	0.3V	13.13	Simulated solar light	[34]
AlaNDI-Ca	150/163	100V	0.65	365	[35]
AlaNDI-Zn	369/505	-	400	785	[36]

2Tpy-Zn CONASH	0.06/0.063	40	13×10^3	450	[37]
P3HT/ZnO	0.09/0.098	0V	125	365	[38]
ZnO/Ni-CAT-3	0.003/0.05	0V	137	450	This work

Note: AlaNDI stands for N, N'-Bis[(S)-1-carboxyethyl]naphthalene-1,8:4,5-bisdicarbimide; 2Tpy stands for bisterpyridine, CONASH stands for coordination nanosheets and P3HT stands for poly(3-hexylthiophene).

The supreme performance of ZnO/Ni-CAT based PD can be further explained by the energy band diagrams, which are illustrated in Figure 5. The work functions (WF, ϕ) of n-type ZnO, p-type Ni-CAT, Au electrode and Ag electrode are 4.0 eV, 5.0 eV, 5.1 eV and 4.26 eV, respectively.[22, 39] The band gap of n-type ZnO and p-type Ni-CAT are 3.31eV and 2.68 eV, respectively.[22, 39] (Figure 5a, c). For ZnO/Ni-CAT-0 based PDs, the ZnO can absorb photogenerated holes due to the BEF (V_{bi}) generated at the Schottky junction of Au/ZnO and Ag/ZnO interface. The Au electrode acted as a hole-trap site, which created free electrons in the conduction band of ZnO during illumination and contributed to the external current. For ZnO/Ni-CAT based PDs, the electrons will transfer from ZnO to Ni-CAT at its hetero-interface due to their different work functions until an equilibrium is reached. When their electronic state reaches equilibrium, the band structure bends upward for ZnO and downward for Ni-CAT at the interface, which forms a heterojunction and a BEF would form because of the bending bandgaps. The differences of WF between ZnO and Ni-CAT generate a BEF of $V_{bi} = 0.78$ and will facilitate the separation of photogenerated carriers. Under illumination, the photogenerated electrons migrated from the conduction band (E_C) of Ni-CAT to ZnO and the photogenerated holes migrated from the valence band of ZnO to Ni-CAT, which produced a photocurrent (Figure 5d). Because of the narrow energy bandgap of Ni-CAT, it can absorb a wide spectrum of illumination, which further promotes its application as broadband PDs.
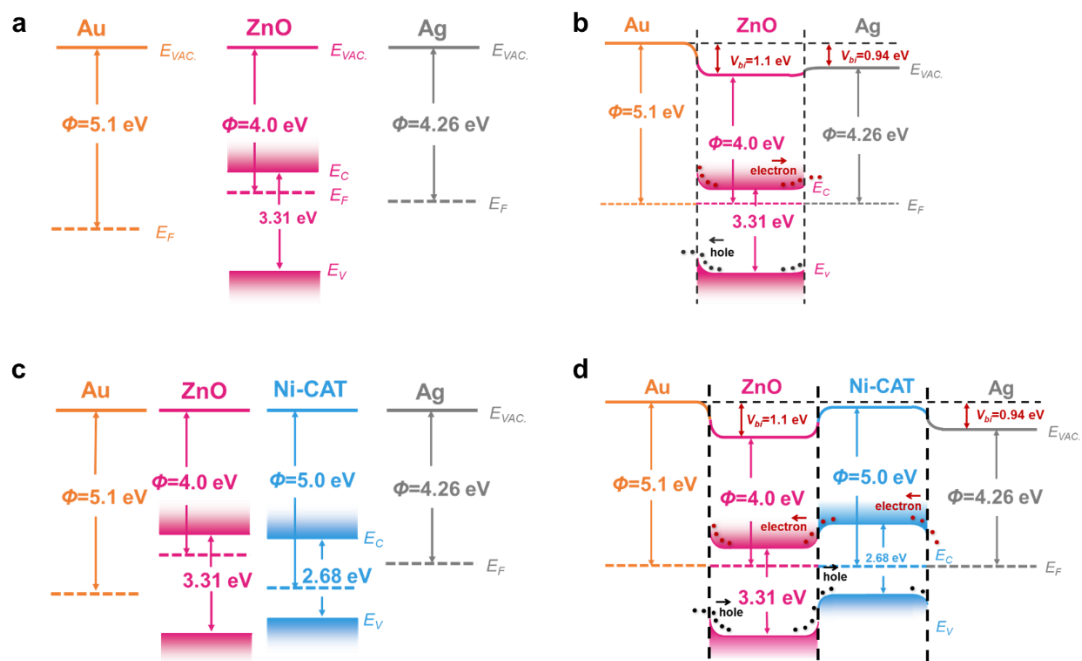
Figure 5. Schematic energy band diagram of pure ZnO and ZnO/Ni-CAT based PDs before (a, c) and after contact (b, d), respectively.

Conclusions

In conclusion, we *in situ* grew the EC-MOF (p-type Ni-CAT) on the surface of n-type ZnO NRs and fabricated a self-powered photodetector formed with their heterojunction nanostructures. Upon 450 nm light illumination and zero bias voltage, the as-fabricated photodetector showed relatively high photoresponse with fast rise and decay times, which can be ascribed to the formed BEF within the established heterojunction. This study not only promotes the development of ZnO/Ni-CAT-3 heterojunction photodetectors but also provides great inspiration for the preparation of other new photovoltaic devices and systems based on MOF materials.

Supporting Information

Synthesis and fabrication process of ZnO/Ni-CAT based PDs, Characterization data of ZnO/Ni-CAT, and results of photoresponse to ZnO/Ni-CAT based PDs.

Acknowledgements

References

(1) Kumar, P.; Kim, K.-H.; Rarotra, S.; Ge, L.; Lisak, G. The Advanced Sensing Systems for NO_x Based on Metal-Organic Frameworks: Applications and Future Opportunities. *TrAC, Trends Anal. Chem.* **2020,** *122*, 115730.

(2) Liu, J.; Wöll, C. Surface-Supported Metal–Organic Framework Thin Films: Fabrication Methods, Applications, and Challenges. *Chem. Soc. Rev.* **2017,** *46*, 5730-5770.

(3) Corma, A.; García, H.; Llabrés i Xamena, F. X. Engineering Metal Organic Frameworks for Heterogeneous Catalysis. *Chem. Rev.* **2010,** *110*, 4606-4655.

(4) Kreno, L. E.; Leong, K.; Farha, O. K.; Allendorf, M.; Van Duyne, R. P.; Hupp, J. T. Metal–Organic Framework Materials as Chemical Sensors. *Chem. Rev.* **2012,** *112*, 1105-1125.

(5) Zhang, X.; Chen, A.; Zhong, M.; Zhang, Z.; Zhang, X.; Zhou, Z.; Bu, X.-H. Metal-Organic Frameworks (MOFs) and MOF-Derived Materials for Energy Storage and Conversion. *Electrochem. Energy Rev.* **2019,** *2*, 29-104.

(6) Zhang, X.; Wang, X.; Fan, W.; Wang, Y.; Wang, X.; Zhang, K.; Sun, D. A multifunctional Zr-MOF for the Rapid Removal of $Cr_2O_7^{2-}$, Efficient Gas Adsorption/Separation, and Catalytic Performance. *Mater. Chem. Front.* **2020,** *4*, 1150-1157.

(7) Tran, Y. B. N.; Nguyen, P. T. K.; Luong, Q. T.; Nguyen, K. D. Series of M-MOF-184 (M= Mg, Co, Ni, Zn, Cu, Fe) Metal-Organic Frameworks for Catalysis Cycloaddition of CO_2. *Inorg. Chem.* **2020,** *59*, 16747-16759.

(8) Stassen, I.; Burtch, N. C.; Talin, A. A.; Falcaro, P.; Allendorf, M. D.; Ameloot, R. An Updated Roadmap for the Integration of Metal-Organic Frameworks with Electronic Devices and Chemical Sensors. *Chem. Soc. Rev.* **2017,** *46*, 3185-3241.

(9) Arora, H.; Dong, R.; Venanzi, T.; Zscharschuch, J.; Schneider, H.; Helm, M.; Feng, X.; Cánovas, E.; Erbe, A. Demonstration of a Broadband Photodetector Based on a Two-Dimensional Metal-Organic Framework. *Adv. Mater.* **2020,** *32*, 1907063.

(10) Hu, S.; Zhang, J.; Chen, S.; Dai, J.; Fu, Z. Efficient Ultraviolet Light Detector Based on a Crystalline Viologen-Based Metal-Organic Framework with Rapid Visible Color Change under Irradiation. *ACS Appl. Mater. Interfaces* **2017,** *9*, 39926-39929.

(11) Xu, W. J.; Zhao, Y. J.; Wang, H. R.; Wang, H. F.; Pan, F. F.; Xu, R. X.; Hou, H. W. Postsynthetic-Modified PANI/MOF Composites with Tunable Thermoelectric and Photoelectric Properties. *Chem. - Eur. J.* **2021,** *27*, 5011-5018.

(12) Zhang, T.; Cao, J. W.; Jiang, X.; Chen, J.; Wang, T.; Chen, K. J. Band Gap Modulation Enabled by TCNQ Loading in a Ru-Based Metal-Organic Framework for Enhanced Near-Infrared Absorption and Photothermal Conversion. *Cryst. Growth Des.* **2021,** *21*, 729-734.

(13) Rodenas, T.; Luz, I.; Prieto, G.; Seoane, B.; Miro, H.; Corma, A.; Kapteijn, F.; Llabres i Xamena, F. X.; Gascon, J. Metal-Organic Framework Nanosheets in Polymer Composite Materials for Gas Separation. *Nat. Mater.* **2015,** *14*, 48-55.

(14) Wang, M.-Q.; Zhang, Y.; Bao, S.-J.; Yu, Y.-N.; Ye, C. Ni(II)-Based Metal-Organic Framework Anchored on Carbon Nanotubes for Highly Sensitive Non-Enzymatic Hydrogen Peroxide Sensing. *Electrochim. Acta* **2016,** *190*, 365-370.

(15) Park, J.; Lee, M.; Feng, D.; Huang, Z.; Hinckley, A. C.; Yakovenko, A.; Zou, X.; Cui, Y.; Bao, Z. Stabilization of Hexaaminobenzene in a 2D Conductive Metal–Organic Framework for High Power Sodium Storage. *J. Am. Chem. Soc.* **2018,** *140*, 10315-10323.

(16) Sun, Y.; Amsler, M.; Goedecker, S.; Caravella, A.; Yoshida, M.; Kato, M. Surfactant-Assisted Synthesis of Large Cu-BTC MOF Single Crystals and Their Potential Utilization as Photodetectors. *CrystEngComm* **2019,** *21*, 3948-3953.

(17) kang, c.; Iqbal, M. A.; Zhang, S.; Weng, X.; Sun, Y.; Qi, L.; Tang, W.; Ruan, S.; Zeng, Y.-J. $Cu_3(HHTP)_2$ c-MOF/ZnO Ultrafast Ultraviolet Photodetector for Wearable Optoelectronics. *Chem. - Eur. J.* **2022,** *28*, e202201705.

(18) Liu, L.; Li, G. H.; Wang, Y.; Wang, Y. Y.; Li, T.; Zhang, T.; Qin, S. J. A Photovoltaic Self-Powered Gas Sensor Based on a Single-Walled Carbon Nanotube/Si Heterojunction. *Nanoscale* **2017,** *9*, 18579-18583.

(19) Yang, L.; He, X.; Dincă, M. Triphenylene-Bridged Trinuclear Complexes of Cu: Models for Spin Interactions in Two-Dimensional Electrically Conductive Metal-Organic Frameworks. *J. Am. Chem. Soc.* **2019,** *141*, 10475-10480.

(20) Hoffmann, M. W. G.; Gad, A. E.; Prades, J. D.; Hernandez-Ramirez, F.; Fiz, R.; Shen, H.; Mathur, S. Solar Diode Sensor: Sensing Mechanism and Applications. *Nano Energy* **2013,** *2*, 514-522.

(21) He, T.; Lan, C.; Zhou, S.; Li, Y.; Yin, Y.; Li, C.; Liu, Y. Enhanced Responsivity of a Graphene/Si-based Heterostructure Broadband Photodetector by Introducing a WS_2 Interfacial Layer. *J. Mater. Chem. C* **2021,** *9*, 3846-3853.

(22) Yoon, J. W.; Jo, Y.-M.; Lee, J.-H. Type-II BiVO$_4$/Ni$_3$(hexahydroxytriphenylene)$_2$ Heterojunction Photoanodes for Effective Photoelectrochemical Reaction. *Energy Adv.* **2022,** *1*, 197-204.

(23) Zhan, W.-w.; Kuang, Q.; Zhou, J.-z.; Kong, X.-j.; Xie, Z.-x.; Zheng, L.-s. Semiconductor@Metal-Organic Framework Core-Shell Heterostructures: A Case of ZnO@ZIF-8 Nanorods with Selective Photoelectrochemical Response. *J. Am. Chem. Soc.* **2013,** *135*, 1926-1933.

(24) Shi, Y. X.; Wu, Y.; Wang, S. Q.; Zhao, Y. Y.; Li, T.; Yang, X. Q.; Zhang, T. Soft Electrochemical Actuators with a Two-Dimensional Conductive Metal-Organic Framework Nanowire Array. *J. Am. Chem. Soc.* **2021,** *143*, 4017-4023.

(25) Zhou, Q.; Zeng, W.; Chen, W.; Xu, L.; Kumar, R.; Umar, A. High sensitive and Low-Concentration Sulfur Dioxide (SO$_2$) Gas Sensor Application of Heterostructure NiO-ZnO Nanodisks. *Sens. Actuators, B* **2019,** *298*, 126870.

(26) Zhou, T.; Cao, S.; Zhang, R.; Tu, J.; Fei, T.; Zhang, T. Effect of Cation Substitution on the Gas-Sensing Performances of Ternary Spinel MCo$_2$O$_4$ (M = Mn, Ni, and Zn) Multishelled Hollow Twin Spheres. *ACS Appl. Mater. Interfaces* **2019,** *11*, 28023-28032.

(27) Zhou, T.; Chen, S.; Wang, X.; Xie, C.; Zeng, D. Catalytic Activation of Cobalt Doping Sites in ZIF-71-Coated ZnO Nanorod Arrays for Enhancing Gas-Sensing Performance to Acetone. *ACS Appl. Mater. Interfaces* **2020,** *12*, 48948-48956.

(28) Li, G.; Lin, L.; Guan, W.; Wei, C.; Sujie, Q.; Yi, W.; Ting, Z. Self-Powered UV-Near Infrared Photodetector Based on Reduced Graphene Oxide/n-Si Vertical Heterojunction. *Small* **2016,** *12*, 5019-5026.

(29) Yan, Z.; Li, S.; Liu, Z.; Zhi, Y.; Dai, J.; Sun, X.; Sun, S.; Guo, D.; Wang, X.; Li, P.; Wu, Z.; Li, L.; Tang, W. High Sensitivity and Fast Response Self-Powered Solar-Blind Ultraviolet Photodetector with a β-Ga$_2$O$_3$/Spiro-MeOTAD p-n Heterojunction. *J. Mater. Chem. C* **2020,** *8*, 4502-4509.

(30) Chen, D.; Xin, Y.; Lu, B.; Pan, X.; Huang, J.; He, H.; Ye, Z. Self-Powered Ultraviolet Photovoltaic Photodetector Based on Graphene/ZnO Heterostructure. *Appl. Surf. Sci.* **2020,** *529*, 147087.

(31) Zheng, Z.; Yao, J.; Zhu, L.; Jiang, W.; Wang, B.; Yang, G.; Li, J. Tin Dioxide Quantum Dots Coupled with Graphene for High-Performance Bulk-Silicon Schottky Photodetector. *Mater. Horiz.* **2018,** *5*, 727-737.

(32) Zheng, Z.; Yao, J.; Yang, G. Centimeter-Scale Deposition of Mo$_{0.5}$W$_{0.5}$Se$_2$ Alloy Film for High-Performance Photodetectors on Versatile Substrates. *ACS Appl. Mater. Interfaces* **2017,** *9*, 14920-14928.

(33) Zeng, L.; Lin, S.; Lou, Z.; Yuan, H.; Long, H.; Li, Y.; Lu, W.; Lau, S. P.; Wu, D.; Tsang, Y. H. Ultrafast and Sensitive Photodetector Based on a PtSe$_2$/Silicon Nanowire Array Heterojunction with a Multiband Spectral Response from 200 to 1550 nm. *NPG Asia Mater.* **2018,** *10*, 352-362.

(34) Luo, S.; Wu, Z.; Zhao, J.; Luo, Z.; Qiu, Q.; Li, Z.; Wu, H.; Xing, G.; Wu, C. ZIF-67 Derivative Decorated MXene for a Highly Integrated Flexible Self-Powered Photodetector. *ACS Appl. Mater. Interfaces* **2022,** *14*, 19725-19735.

(35) Shang, X.; Song, I.; Jung, G. Y.; Choi, W.; Ohtsu, H.; Lee, J. H.; Ahn, J.; Koo, J. Y.; Kawano, M.; Kwak, S. K. Micro-/Nano-Sized Multifunctional Heterochiral Metal–Organic Fameworks for High-Performance Visible–Blind UV Photodetectors. *J. Mater. Chem. C* **2021,** *9*, 7310-7318.

(36) Shang, X.; Song, I.; Jung, G. Y.; Choi, W.; Ohtsu, H.; Lee, J. H.; Koo, J. Y.; Liu, B.; Ahn, J.; Kawano, M. Chiral Self-Sorted Multifunctional Supramolecular Biocoordination Polymers and Their Applications in Sensors. *Nat. Commun.* **2018,** *9*, 3933.

(37) Khan, A.; Xiang, S.; Zhou, Z.; Zhu, C.; Zhang, W.; Han, G.; Jiang, K.; Li, D.; Pan, A.; Weng, Q. Bottom-Up Fabrication of Semiconducting 2D Coordination Nanosheets for Versatile Bioimaging and Photodetecting Applications. *Mater. Adv.* **2021,** *2*, 5189-5194.

(38) Ouyang, B.; Zhang, K.; Yang, Y. Self-Powered UV Photodetector Aarray Based on P3HT/ZnO Nanowire Array Heterojunction. *Adv. Mater. Technol.* **2017,** *2*, 1700208.

(39) Yuan, K.; Chen, L.; Li, F.; Chen, Y. Nanostructured Hybrid ZnO@CdS Nanowalls Grown In Situ for Inverted Polymer Solar Cells. *J. Mater. Chem. C* **2014,** *2*, 1018-1027.

Table of Contents (TOC)
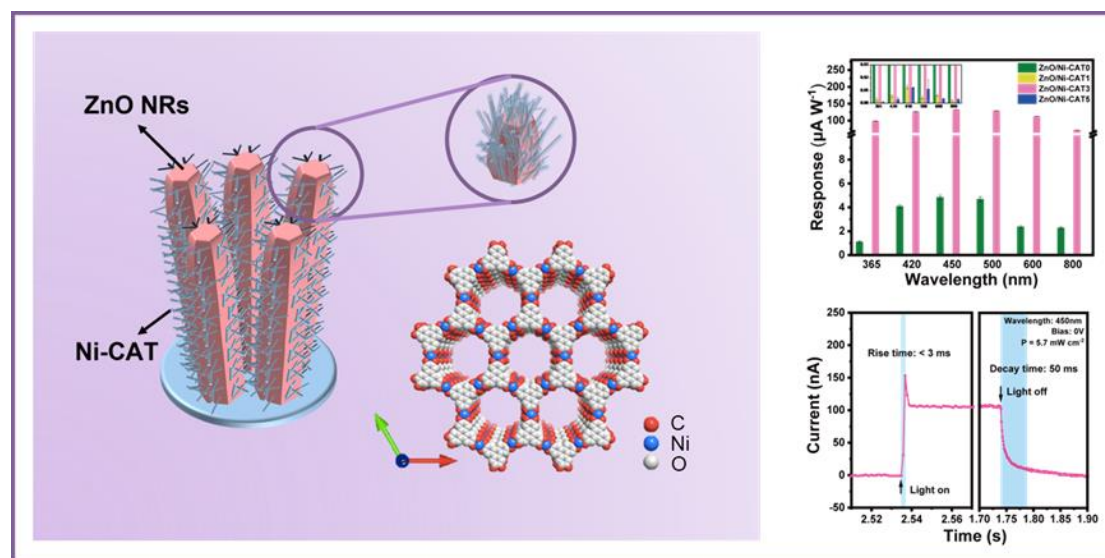
Schematic diagram of ZnO/Ni-CAT heterojunction based PDs with their photo-sensing performance.